



ASME Accepted Manuscript Repository

Institutional Repository Cover Sheet

Budimir

Rosic

*First*

*Last*

ASME Paper Title: Investigation of Unsteady Flow Phenomena in First Vane Caused by Combustor Flow With Swirl

Authors: Simon Jacobi, Cosimo Mazzoni, Budimir Rosic and Krishan Chana

ASME Journal Title: Journal of Turbomachinery

Volume/Issue 139/4 Date of Publication (VOR\* Online) Jan 10, 2017

ASME Digital Collection URL: <http://turbomachinery.asmedigitalcollection.asme.org/article.aspx?articleid=2579723>

DOI: 10.1115/1.4035073

\*VOR (version of record)

# **Investigation of Unsteady Flow Phenomena in First Vane Caused by Combustor Flow with Swirl**

**Simon Jacobi<sup>?</sup> Cosimo Mazzoni Budimir Rosic**

Osney Thermo-Fluids Laboratory  
Department of Engineering Science  
University of Oxford  
Oxford OX2 0ES, United Kingdom  
<sup>?</sup>Email: [simon.jacobi@eng.ox.ac.uk](mailto:simon.jacobi@eng.ox.ac.uk)

**Krishan Chana**

Whittle Laboratory  
Department of Engineering  
Cambridge University  
Cambridge CB3 0DY, United Kingdom

## **ABSTRACT**

The flow at the combustor turbine interface of power generation gas turbines with can combustors is characterized by high and non-uniform turbulence levels, lengthscales and residual swirl. These complexities have a significant impact on the first vanes aerothermal performance and lead to challenges for an effective turbine design. To date, this design philosophy mostly assumed steady flow and thus largely disregards the intrinsic unsteadiness. This paper investigates the steady and unsteady effects of the combustor flow with swirl on the turbines first vanes. Experimental measurements are conducted on a high-speed linear cascade that comprises two can combustors and four nozzle guide vanes. The experimental results are supported by a Large Eddy Simulation performed with the inhouse CFD flow solver TBLOCK. The study reveals the highly unsteady nature of the flow in the first vane and its effect on the heat transfer. A persistent flow structure of concentrated vorticity is observed. It wraps around the unshielded vane's leading edge at midspan and periodically oscillates in spanwise direction due to the interaction of the residual low-pressure swirl core and the vane's potential field. Moreover, the transient behavior of the horseshoe-vortex system due to large fluctuations in incidence is demonstrated.

## INTRODUCTION

Lean-Premixed (LPM) combustors are broadly used in industry due to their superior emission characteristics compared to conventional rich-burn combustors. Stringent regulations are set for the goal of reducing  $\text{NO}_x$  emissions due to their detrimental effects and LPM combustion promises to offer the highest potential for  $\text{NO}_x$  reduction [1]. This is achieved by LPM combustor's architecture, in which different configurations of swirl injectors generate a lean mixture of fuel and air prior combustion. This results in lower temperatures and thus lower  $\text{NO}_x$  emissions compared to conventional rich-burn combustors.

The aerodynamic behavior of fluids within LPM combustors is greatly influenced by swirl generators, and an overview of different configurations and designs can be found in [2]. They are employed to provide effective mixing due to strong shear regions and high turbulence [3] [4]. The fluid exiting the swirl generators typically shows three flow structures [2]. A recirculation zone develops in the center due to vortex breakdown which causes an adverse pressure gradient. A Precessing Vortex Core (PVC) is often observed at a certain frequency around the former recirculation zone [5]; the frequency of precession depends on the burner/swirl configuration and increases linearly with flow rate [6]. Furthermore, corner recirculation zones establish when the main flow exiting the swirl generators encounters the ambient fluid, leading to shear layers due to velocity gradients and thus to vortex structures.

The complex flowfield produced by LPM combustors leads to aerothermal challenges for the turbine. The temperature profile is non-uniform due to the discrete number of combustors which also results in hot streaks and can lead to thermal problems. This challenge is intensified by the continuous strive for higher turbine inlet temperatures to increase thermal efficiency as well as further thermal stress at the endwalls due to the flatter temperature profile of LPM combustors (due to more effective mixing). Aerodynamic challenges occur due to high and non-uniform turbulence intensities and lengthscales, and non-uniform pressure (ie. PVC) and velocity profiles (ie. residual swirl, boundary layers) which significantly affect heat transfer, secondary flows and film cooling within the turbine.

First vanes are often designed considering combustor and turbine as two isolated components. In order to analyse the effect of the combustor on the turbine, an integrated approach comprising the combustor and the vanes of the HP turbine is presented. Previous studies have already investigated the coupling of combustor and HP turbine with different levels of sophistication. Investigations by Qureshi et al. [7] [8] on an HP turbine reported significant spanwise variations in heat flux between a uniform and a swirling flow at the inlet. However, it has been shown that the use of simple inlet profiles for turbine development does not do justice to the complex flowfield - with turbulence levels and lengthscales as high as 35% (of  $\bar{v}_x$ ) and 25% (of  $c_x$ ) respectively [9] - exiting the combustor [10]. Ames et al. [11] demonstrated that an increase in turbulence intensity (of 4%) hastens boundary-layer transition and increases the Stanton number (of up to 20%) on the vane. Inlet swirl also influences the heat transfer [12] and hot-streak migration [13] by leading to a radial migration (depending on swirl direction) of the hot fluid within the NGV passage and thus considerably influencing the aerothermal performance. An inadequate representation of the vane inlet can thus lead to poor performance of the HP turbine and result in thermal fatigue. Similarly, the high pressure turbine influences the upstream behavior of the flowfield in the combustor [10]. Modeling the combustor and the HP turbine simultaneously (or at least loosely coupling them [12]) should thus replace an individual

---

assessment.

Furthermore, it is common practice to use steady CFD as a design tool. Although steady methods may capture some basic flow features, turbomachinery flows are naturally unsteady. In fact, the evidence of instability in swirl combustion systems has been extensively reported in literature [2] [6]. There are also a few studies which quantify the processes occurring under PVC driven oscillations for representative but very different conditions, using a variety of experimental techniques [14] [15] and numerical approaches [16] [17]. Therefore, unsteady flow simulations seem to be needed to characterise the complex mechanisms occurring in LPM combustors, to properly investigate the effect of inlet non-uniformities in gas turbines, and to capture the correct physics of hot-streak migration [18]. Cha et al. [10] furthermore highlight that modeling NGV passages with LES instead of two-equation RANS models could be beneficial for simulating the turbulence. You et al. [19] performed an integrated simulation including fan, compressors, turbines (URANS) and combustor (LES) for a 20° sector of a Pratt & Whitney gas turbine engine and illustrated that the flow exiting the combustor features fine-scale velocity fluctuations and intermittent large-scale flow structures.

While You's study includes chemical reactions, they are omitted by others [20] [21] [22]. The chemical reactions occurring during combustion influence the flowfield within the combustor downstream of the swirl-injectors [23] [24]. It is reported that the precessing vortex core and vortex breakdown will likely differ between a reacting and a non-reacting scenario for high swirl and diffusive flows [25] [26] [27] [28]. The oscillations of the PVC can potentially also be suppressed by combustion, as illustrated by Selle et al. [29]. This difference is due to the instability caused by heat-release in the reacting case. This lack of heat-release in the non-reactive case imposes challenges for the goal of achieving engine representative swirl- and temperature-distributions as target combustor outlet profiles simultaneously.

A comprehensive overview of the research on unsteady pressure, temperature and turbulence in combustors is given by Lubbock [30]. Current research suggests that exit turbulence is primarily a result of combustor geometry, swirl and secondary flows [31], and the combustion process does not appear to have a significant impact [32] [33]. The level of swirl is however affected by combustion, with which it appears to decrease [23]. Turbulence intensity may therefore be reduced by combustion depending on the level of swirl responsible for the turbulence.

All this suggests that a form of unsteadiness, depending on the combustor geometry and process, could potentially occur at the combustor-turbine interface. The effect of this unsteadiness on the downstream turbine is not, as yet, well understood. This paper thus aims to describe and discuss the steady and unsteady effects of engine realistic combustor flow (non-reactive with uniform temperature) on the vane's aerothermal behavior observed in experiments and numerical simulations. It is shown that the interaction of a residual swirl core (region of high swirl, and low total and static pressure) and the vane potential field leads to the formation of a spanwise-fluctuating flow structure around the vane's leading edge. Moreover the paper shows the highly unsteady nature of the horse-shoe vortex with pitchwise fluctuations of the passage vortex caused by the large time-dependent variations in incidence. These two unsteady phenomena are schematically illustrated in Figure 1.



---

## EXPERIMENTAL FACILITY

The experimental facility used in this study for aerothermal investigations at the combustor-turbine interface is a linear cascade operated at scaled engine conditions [34]. It is a blown-down type facility that is high subsonic, non-rotating, and nonreactive. Figure 2 shows the CAD geometry and a photo of the experimental facility. It models two can combustors including swirl-generators and transition duct, four high-pressure nozzle guide vanes, and tailboards (not shown) for flow periodicity. The facility is highly modular and allows quick changes of the flow conditions by exchanging cassettes upstream of the transition ducts. Three different cassettes allow to test a swirl scenario, reversed swirl scenario and no-swirl scenario. The no-swirl scenario constitutes an upstream turbulence grid that results in 12% turbulence intensity (estimated through empirical correlations by Roach [35]) and the swirlers result in an averaged swirl angle ( $\tan^{-1}(\frac{V_{\text{tangential}}}{V_{\text{axial}}})$ ) of  $8^\circ$  at the inlet of the vanes.

Aerodynamic measurements include up- and downstream (of the vane) automated area traverse measurements with a 5-hole probe (2.05mm head diameter and 0.3mm hole diameter; estimated uncertainty to within 95% confidence of 0.35 [34]). Thermal measurement methods used in this study include infrared camera measurements and thin-film-gauge measurements. Heat transfer coefficient (HTC) distributions are obtained from the infrared camera measurements by using Oldfield's impulse response method [36]. A 4.87% HTC accuracy is achieved for an idealized heat transfer process when taking into account the uncertainty of the infrared camera measurements, material properties and the  $q - T_w$  least-squares fit [34]. One of the unshielded vanes was instrumented with a total of 41 Thin Film Heat Flux Gauges (TFHFGs) [37] and seven K-type thermocouples. The distribution of gauges on the vane was based on numerical predictions in order to capture the unsteady flow phenomena investigated. The differential voltage signals across each gauge were amplified using a Heat Transfer Amplifier originally designed by Oldfield [36]. The heat flux across the insulating layer was calculated using the semi-infinite one-dimensional heat conduction model [38] and computed using Oldfield's impulse response method [36].

Table 1 summarizes the operating conditions in the experimental facility. An upstream total pressure of 1.6 bar and a massflow rate of  $4.8 \frac{\text{kg}}{\text{s}}$  is achieved by a pressure regulator and a critical flow Venturi nozzle fed by a high-pressure reservoir at ambient temperature. A vane pressure ratio of  $\frac{P_2}{P_{01}}=0.75$  results in an average exit Mach number of 0.65 ( $M_{\text{peak}} = 0.85$ ) which represents an engine-realistic high-velocity flow condition. A Reynold's number of  $1.6 \cdot 10^6$  (based on axial chord at midspan) is obtained. A heater-mesh, used for heat transfer measurements, provides a step-rise in mainstream temperature of approximately 30 °C by dissipating 150 kW of DC power. The flow is finally exhausted to the atmosphere.

## NUMERICAL METHODOLOGY

Numerical simulations were performed using the in-house flow solver TBLOCK developed by John Denton [39]. It solves the unsteady, compressible, three-dimensional governing equations in a cylindrical coordinate system using the finite volume method with cell corner storage of the flow variables. The multiblock nature of TBLOCK allows the efficient treatment of complex geometries. To reduce the computation time and enable large-scale computations the code was parallelised using MPI. Different LES models were implemented by Klostermeier [40]. To march the flow forward in time, TBLOCK offers an explicit scheme and the implicit dual time stepping algorithm. Although the higher accuracy of the explicit scheme

for LES is desirable, investigations have shown that the resulting small time step imposed by the CFL conditions is too restrictive for industrial applications [40]. For this reason all simulations were conducted using the dual time stepping method which allows the use of acceleration techniques such as multigrid and local time stepping. The WALE sub-grid scale (SGS) model was used for the LES. The steady simulations used the mixing length approach (which allows the tuning of two parameters, namely the free stream turbulence level and the free stream mixing length) as a turbulence model which was calibrated against experimental measurements for this study. Heat transfer prediction capabilities and temperature wall functions were implemented by Mazzoni [41].

The computational domain for LES, comprising of swirler, transition duct and two nozzle guide vanes, is shown in the schematic of Figure 3. The structured mesh consists of 857 blocks and 120 million elements. This results in an inlet node-count of width height = 300 300, a swirler-vane resolution of span pitch = 70 80 and an NGV resolution of span pitch = 170 180. The mesh is illustrated by a horizontal cut through the swirler and the vane passage. The domain for the steady simulations (also shown in Figure 3) only includes the vane passage and has a mesh size of 4.3 million elements. The LES uses a constant total pressure inlet in the duct upstream of the swirler and a static pressure outlet downstream of the vanes, while the steady CFD uses distributions of total pressure, yaw and pitch (obtained from upstream aerodynamic traverse measurements) as inlet and static pressure as an outlet boundary condition.

The LES simulations were performed on 224 cores (Intel E5-2640v3 Haswell; 64GiB-128GiB per node) of the Oxford Super Computer. 50000 iterations of steady RANS are used as an initialization and the Large-Eddy-Simulation was run for 20 cycles (a cycle corresponds to one convection pass) through the domain. Each cycle is subdivided into 6000 outer steps and corresponds to a physical time of 20ms. The averaging of the flow variables was conducted for the time of one convection pass.

## INVESTIGATION OF COMBUSTOR FLOW

A generic swirler was developed to generate the same flow features as engine realistic combustor geometries. A bypass around the pilot swirler and a diffusion duct strengthen the extent of the recirculation zone. The swirler is designed to achieve a mass-averaged swirl angle of 8° (clockwise when looking upstream) at the end of the transition duct. More detailed information on the geometry and development of the swirler can be found in [42]. A second swirler with reversed swirl direction (anti-clockwise when looking upstream) is obtained by mirroring the swirler on a vertical plane.

Figure 4 shows the flow domain downstream of the swirler in one can combustor and two downstream vanes, and an iso-surface of total pressure - obtained from an instantaneous time step of the LES - is used to illustrate this flowfield. Downstream of the swirler (1) a low pressure zone establishes and leads to an area of flow reversal, the recirculation zone (2). This is intended in combustors to increase residence times and thus flame stability. The residual swirl core (3) is convected through the transition duct in a precessing motion, indicating the unsteadiness of the combustor flow and the core's spatial fluctuation. It is then deflected by the unshielded conventional vane's leading edge stagnation pressure region (4). Most of the residual swirl core is convected along the suction side and a smaller part along the pressure side, which is specific for the clocking position in this study (with one shielded vane and one vane in the center of the passage).

Figure 5 shows the energy cascade for a point upstream of and in the middle of the nozzle guide vanes at midspan (also see schematic). It was obtained by calculating the Power Spectral Density of the fluctuating velocity component during one convection pass. It can be seen that the LES is able to resolve the lengthscales of the energy containing eddies for both points. This gives further confidence to the validity of the numerical results.

Figure 6 shows the time-averaged turbulence intensity,  $I$ , within the transition duct and the vane passages at midspan for three different pitchwise positions, see 'passage 1', 'central' and 'passage 2' in schematic. The central line shows the highest turbulence intensities due to the high velocity fluctuations in the swirler's wake. It can be seen that the turbulence intensity decays along the transition duct as the unstable large scale structures (initially comparable in size to the swirler-vanes) break up into smaller eddies. The turbulence intensity of approximately 10%-20% at the inlet of the vanes drops significantly due to the acceleration and convection of the flow through the vane passages.

## CONVECTION OF RESIDUAL SWIRL CORE

A set of experimental and numerical investigations were undertaken to obtain a better understanding of the convection of the combustor flow through the transition duct and vane passages. Aerodynamic traverse measurements were conducted up- and downstream of the nozzle guide vanes to illustrate the migration of the residual swirl core and its effect on the vane's aerodynamic performance.

Figure 7 shows the total pressure (non-dimensionalised by total pressure in duct)  $\bar{p}_0$ , yaw and pitch angle distributions downstream of the transition duct obtained through traverse measurements with installed swirler. A pronounced low-pressure core in the center is apparent, with areas of high total pressure in the top left and bottom right corners. The white arrows in the yaw and pitch contours indicate the global velocity direction in this region. Combining both plots illustrates the residual swirl. The swirl thus leads to positive yaw (in the direction of the vane turning) in the upper half and to negative yaw in the lower half of the domain. The azimuthal velocity of the residual swirl leads to a pressure gradient ( $\frac{dp}{dr} = \frac{r u_\theta^2}{r}$ ) due to centrifugal forces and thus to a low static pressure core (similar to the low total pressure core in Figure 7) in the center. Traverse measurements of the reversed swirl case were also conducted and their distributions can be obtained by mirroring these plots on a vertical axis and switching the velocity directions of pitch and yaw.

Figure 8 shows the dimensionless total pressure ( $\bar{p}_0$ ) and yaw downstream of the nozzle guide vanes obtained through traverse measurements with the swirler installed. The wake downstream of the shielded vane shows a higher loss compared to the unshielded vane due to the presence of the upstream combustor wall. Furthermore it can be seen that the hub loss core of the unshielded vane is larger than the casing loss core and is shifted tangentially to the left. The former will be explained later in the paper, the latter is due to the hub loss core's convection downstream at an under-turned flow angle (see reduced turning towards hub as compared to casing in Figure 8) due to the negative yaw upstream of the vanes (see Figure 7). Moreover the measurements show that the high total pressure zones in the corners upstream of the vanes are convected through the passage, and can still be seen downstream of the vanes on the unshielded vane's pressure side towards the hub and the suction side towards the casing.

Figure 9 shows a comparison of pitchwise averaged dimensionless total pressure ( $\bar{p}_0$ ) and yaw downstream of the

---

nozzle guide vanes between experimental measurements and time-averaged LES with the swirler installed upstream of the transition duct. The spanwise total pressure plot confirms that the hub loss core is more pronounced than the casing loss core, and migrates radially further from the endwall. Turning close to the hub is approximately 2° lower than close to the casing due to the upstream negative yaw towards the hub. Qualitative and quantitative agreement between experimental measurements and time-averaged LES is found to be good with slightly under-estimated total pressure loss around midspan by the LES and deviations in turning of less than 1°.

Figure 10 shows a schematic description of the interaction between the residual swirl core and the unshielded vane's potential field. The total pressure deficit in the duct's center (caused by the swirler's wake) results in a non-uniform velocity field and the low momentum fluid close to midspan is turned quicker by the vane potential field than the high momentum fluid further from midspan. This leads to vorticity at the vane's leading edge, with the flow 'rolling-up' towards midspan (see red and blue arrows in Figure 10a). This is analogous to the formation of the horse-shoe vortex. Two counter-rotating structures (red and blue in Figure 10b and c) start to form and are convected to pressure and suction side. On the vane's pressure side of the swirl case, the blue structure's rotation is in line with the residual swirl's orientation (black arrows) and is thus strengthened while the red structure is weakened due to opposing orientations. On the vane's suction side on the other hand, the red structure's rotation is congruent with the residual swirl's orientation and is thus strengthened while the blue structure is weakened. The opposite trends are observed for the reversed swirl case and analogous reasoning can be applied. Figure 10b also shows an instantaneous  $\lambda_2$  iso-surface of the LES, and the two flow structures around the unshielded vane's leading edge can be seen. The structures are often more distorted than in the schematic under the influence of incoming coherent structures and the flow's unsteadiness.

The residual swirl also influences the static pressure distribution in the vane passage, and the stagnation line on the unshielded vane's leading edge, as shown in Figure 11. The no-swirl case results in vertical constant static pressure lines and a vertical stagnation line on the leading edge. The swirl case (Figure 11b) leads to a positive incidence angle at the hub which shifts the stagnation point towards the pressure side, causes increased flow acceleration towards the suction side and thus a region of low static pressure establishes. The flow's acceleration towards the pressure side is reduced at the hub which leads to an increase in static pressure. At the casing, the swirl results in a negative incidence angle which shifts the stagnation point towards the suction side, leads to a reduced acceleration towards the suction side and thus an increase in static pressure. This redistribution of the flow due to swirl leads to a spanwise pressure gradient. The reversed swirl (Figure 11c) leads to a low static pressure zone on the vane's suction side at the casing and the stagnation line is shifted in opposite directions to the swirl case and the corresponding reasoning can be applied. Again, this leads to a spanwise pressure gradient.

The radial pressure gradient introduced in the vane passage due to the residual swirl influences the convection of the remaining flow through the passage. The flow structures described in Figure 10, which resulted from the interaction of the residual swirl core and the vane potential field, are accelerated on the unshielded vane's suction side and, in the swirl case, migrate towards the hub due to the negative pressure gradient (as seen in Figure 11b). This can be seen by the streamtraces in Figure 12a which shows an axial cut of dimensionless total pressure at the vanes trailing edges. It can be seen that the streamtraces originating from the residual swirl core, and the secondary flow streamtraces originating from the upstream

---

hub endwall boundary layer, meet at the trailing edge. Together they form the hub loss core. This explains the reason for the more pronounced hub loss core and its increased radial displacement from the hub endwall as seen in Figure 8. For the reversed swirl case of Figure 12b, the opposing spanwise pressure gradient leads to a pronounced casing loss core for analogous reasons. Furthermore it can be seen that the shielded vane's wake is more symmetric since it is less subjected to the residual swirl and upstream low-pressure core.

## HEAT TRANSFER OF VANE SURFACES

Experimental measurements were conducted to understand the influence of the residual combustor flow with swirl on the vanes thermal performance. Figure 13 shows the steady heat transfer coefficient distributions on the vanes suction surfaces for a swirl and a reversed swirl scenario. The contours were obtained by experimental measurements (using the infrared camera) and steady CFD simulations. The footprint of the secondary flow migration can be seen. The contours show that the separation lines caused by secondary flow on the suction surfaces are radially shifted upwards for a swirl, and downwards for a reversed swirl scenario (compared to a no-swirl case that leads to horizontally symmetric HTC distributions). The steady CFD simulations clearly show the interaction between the flow structure of Figure 10 originating from the residual swirl core with the secondary flow on the unshielded vane's suction surface towards the trailing edge, as illustrated in Figure 12. As expected the shielded vane does not exhibit this phenomenon and the heat transfer coefficient distributions are more symmetric. The same behavior can also be seen in the experimental measurements but the distributions are more diffused indicating that the interaction might be an unsteady phenomenon and its location spatially varying. Overall, qualitative and quantitative agreement between experimental measurements and CFD simulations is found to be good.

## UNSTEADY FLOW PHENOMENA ON VANE SURFACE

Experimental and numerical studies were undertaken to investigate the unsteadiness in the vane passages caused by the combustor flow. To obtain a better qualitative understanding of the complex flowfield, its unsteadiness and the time-dependent behavior of vortical structures in the transition duct and the NGV passages, a visual representation using the lambda 2 criterion is used. Mathematically, lambda 2 is defined by the negative of the second eigenvalue of the symmetry square of the velocity gradient tensor [43]. Unlike the pressure-minimum criterion, it can capture vortex cores at low Reynolds numbers. At the same time it identifies them for high Reynolds numbers by finding the pressure minimum on the plane perpendicular to the vortex axis [44].

Figure 14 shows the wall shear stress on the unshielded vane's suction surface and a transparent iso-surface of the lambda 2 criterion for three different time steps during a cycle. The lambda 2 iso-surface is able to illustrate how the interaction of the residual swirl core with the vane's leading edge potential field leads to the formation of a coherent structure of concentrated vorticity, similar in the development to the formation of secondary flows. The formation of this coherent structure can also be seen in the steady CFD (Figure 13 for example) and to a reduced extent also in steady simulations with only the low total pressure core (without swirl) as an inlet condition (although not shown in this paper). The coherent structure is subsequently convected downstream on the suction and pressure side. It moves radially up and down the leading

---

edge and suction surface, only sometimes interacting with the hub secondary flow. A pronounced effect of this phenomenon on the shear stress, and thus heat transfer, is evident. The transient nature of the residual swirl core helps to explain why the experimental measurements of the heat transfer coefficient distributions in Figure 13 were more diffused than the steady CFD suggested. Plotting the shear stress over the time of one cycle for a point on the leading edge shows fluctuations around the mean of more than 50%. Similar fluctuations in the shear stress are also evident on the pressure surface and its relative amplitudes are even higher (partly in excess of 100%) due to the overall lower heat transfer levels. These fluctuations could have a significant impact on component life and explain the existence of burned spots on the vane surfaces whose occurrence has been ambiguous.

In order to validate these fluctuations in heat transfer, experimental measurements using a vane equipped with TFHFGs were conducted. Figure 15 shows the Discrete Fourier Transformation (DFT) of the temperature of three thin-film gauges for a no-swirl, swirl and reversed swirl scenario. The DFT analyses the frequency and amplitude content of a signal. The measurements indicate that the main content of the fluctuations is well below 1000Hz. All three selected gauges on leading edge, pressure and suction side consistently show the same phenomenon: No dominant frequency beside the constant offset at 0Hz for the no-swirl scenario. However with a swirler installed upstream of the transition duct, all gauges show a pronounced peak in amplitudes at a frequency of approximately 300Hz. This peak occurs for both swirl directions.

Figure 16 shows the DFT of the heat flux on the unshielded vane for three different points on leading edge, pressure and suction side, obtained from the LES with upstream swirler. The heat flux was recorded for every time step for three cycles which only allows a frequency resolution of 8Hz due to the very high sampling rate of 300'000. Nonetheless it can be clearly seen that all three points show a pronounced peak of the amplitudes at approximately 300Hz, thus agree well with the experimental measurements presented in Figure 15 and confirm the existence of the flow phenomena described in Figure 10.

## UNSTEADY FLOW PHENOMENA ON ENDWALL

In this section the influence of combustor flow on the endwall region is presented. It is dominated by secondary flows such as the horse-shoe vortex formation and the migration of the passage vortex. Figure 17 shows an iso-surface of the lambda 2 criterion in the vane passage at two different time steps within a cycle. The first picture indicates how the unshielded vane's pressure side leg horse-shoe vortex forms the passage vortex, migrates towards the adjacent vane's suction side and interacts with the shielded vane's suction side leg horse-shoe vortex, as illustrated by textbook examples of secondary flows. The second picture on the other hand shows, at a subsequent time step, how the passage vortex separates from the adjacent vane's suction side, and nearly contacts its own pressure side. It is convected through the passage without interacting with the shielded vane.

This can be better understood when looking at the (time-dependent) spanwise distribution of flow turning upstream of the vanes, as seen in Figure 18. Temporal fluctuations in yaw (grey area) as high as 15° are superimposed onto the mean turning (red line, black dots). The change in yaw over time is shown by the graphs at 10%, 50% and 90% of the span. These oscillations of turning - at the frequency of the residual swirl core - close to the endwalls lead to a considerable

---

change in momentum and incidence angle, and thus periodically modify the convection of the horse-shoe vortex through the passage. Moreover it is likely that the combustor wake and large turbulence structures that are convected downstream from the combustor interact with the horse-shoe vortex but more detailed investigations are required for a thorough understanding of this phenomenon.

The convection of the horse-shoe vortex through the passage also influences the behavior of the flow downstream of the vanes. Figure 19 shows an iso-surface of the  $\lambda_2$  criterion at three different time steps. In the first instance the passage vortex joins the adjacent vane's horse-shoe vortex and is convected up the suction surface, as expected. However in the second instance the passage vortex does not migrate across the passage. It stays attached to its own vane's pressure side (as in Figure 17) and interacts with the unshielded vane's wake. In the third instance the passage vortex stays away from the adjacent vane, remains attached to the endwall, and finally interacts with the shielded vane's wake.

The LES, validated by experimental measurements, thus suggests a highly unsteady nature of the flow on the vane surfaces and endwalls as a result of an incoming engine realistic combustor flow. Conventional design philosophy, which is in most instances based on steady CFD and an individual assessment of components, is not capable of capturing these unsteady flow interactions. This raises the question of the impact on the component life since the unsteadiness of the flow around the vane surfaces (ie. LE flow structures) and endwalls (ie. horse-shoe vortex) leads to a considerable alteration in the heat transfer and might cause a periodic removal of the film cooling.

## CONCLUSION

This paper investigated the influence of engine realistic combustor flow (non-reactive and uniform temperature) with swirl on the steady and unsteady aerothermal response of the high-pressure turbines nozzle guide vanes. Experimental measurements were performed on a high-speed linear cascade comprising of two can combustors and four nozzle guide vanes. Traverse measurements illustrated the effect of a swirl-generator on the total pressure, pitch and yaw angle distributions up- and downstream of the vanes. It was shown how the swirl leads to a flow redistribution and a resulting radial static pressure gradient. The residual swirl core interacts with the unshielded vane's potential field and a coherent structure of concentrated vorticity forms around the leading edge. This structure is convected along the unshielded vane's pressure and suction side and migrates in radial direction due to the radial static pressure gradient caused by swirl. Towards the unshielded vane's trailing edge it interacts with the secondary flows at the hub or at the casing for a swirl and reversed swirl scenario respectively. The trace of the flow structure originating from the residual swirl core can also be seen on the unshielded vane's heat transfer coefficient distribution, in the experimental measurements as well as in the numerical results.

A Large Eddy Simulation was performed with the inhouse code TBLOCK to qualitatively investigate the unsteady behavior in the vane passage caused by the combustor flow with swirl. It was illustrated how the coherent structures originating from the residual swirl core are convected along the vane surfaces and oscillate harmonically in spanwise direction. A strong influence on the vane's heat transfer was shown. To capture the fluctuations in heat flux on the vane surfaces experimentally, the vane was equipped with 41 Thin-Film Heat Flux Gauges, mainly located on the vanes leading edge, pressure and suction side. Experiments were conducted for a no-swirl, swirl and reversed swirl scenario. A Discrete Fourier Transformation of

---

the heat flux measurements illustrated no dominant frequency for the no-swirl scenario and a pronounced peak in amplitudes at approximately 300Hz for the swirl and reversed swirl scenario. The Discrete Fourier Transformation of the heat flux obtained from the LES similarly showed a clear peak in amplitudes at around 300Hz and thus confirmed the experimental measurements.

The unsteadiness of the horse-shoe vortex was illustrated by the LES. The passage vortex migrates in pitchwise direction through the entire vane passage and only at times interacts with the adjacent vane's horse-shoe vortex. It was shown that this unsteadiness is caused by the residual swirl core's oscillations causing large fluctuations in incidence and upstream pitchwise momentum. Moreover it was suggested that vortical structures emanating from the combustor interact with the horse-shoe vortex and modify its convection through the vane passage.

This paper experimentally and numerically illustrated the highly unsteady nature of the flowfield at the combustor-turbine interface and encourages further investigations for a better physical understanding of these complex interactions and their influence on component life.

#### Acknowledgements

The authors thank Mitsubishi Heavy Industries for supporting this work and Wesley Ramm for his help with measurement techniques. The authors furthermore acknowledge the use of the University of Oxford Advanced Research Computing (ARC) [45] facility in carrying out this work.



## Nomenclature

BL	Boundary layer
DFT/FFT	Discrete/Fast Fourier Transformation
HP	High Pressure
HTC	Heat Transfer Coefficient
LE/TE	Leading Edge / Trailing Edge
LES	Large-Eddy-Simulation
LPM	Lean Premixed
NGV	Nozzle Guide Vane
q	Heat flux per unit area, W=m <sup>2</sup>
T <sub>w</sub>	Surface temperature, K
$\bar{p}_0$	Dimensionless total pressure $\frac{p_0}{[p_0]_{\text{Transition Duct}}}$
PVC	Precessing Vortex Core
(U)RANS	(Unsteady) Reynolds-Averaged Navier-Stokes
SS/PS	Suction Surface / Pressure Surface
Stanton number	$St = \frac{Nu}{Re Pr}$
Swirl Angle	$\tan^{-1}(\frac{v_{\text{tangential}}}{v_{\text{axial}}})$
TFHFG	Thin Film Heat Flux Gauge
Turbulence intensity	$I = \frac{\sqrt{\overline{u'^2 + v'^2 + w'^2}}}{U} = \frac{1}{U} \sqrt{\frac{1}{2}(\overline{u'^2} + \overline{v'^2} + \overline{w'^2})}$

## References

- [1] Lazik, W., Doerr, T., Bake, S., Bank, R., and Rackwitz, L., 2008. "Development of lean-burn low-nox combustion technology at rolls-royce deutschland". Proceedings of the ASME Turbo Expo GT2008-51115.
- [2] Huang, Y., and Yang, V., 2009. "Dynamics and stability of lean-premixed swirl-stabilized combustion". Progress in Energy and Combustion Science, 35(4), pp. 293 – 364.
- [3] Lefebvre, A., 1999. Gas Turbine Combustion. Combustion: An International Series. Taylor & Francis.
- [4] Alekseenko, S. V., Kuibin, P. A., and Okulov, V. L., 2007. "Theory of concentrated vortices". Springer, Berlin/Heidelberg, pp. 309–378.
- [5] Anacleto, P. M., Fernandes, E. C., Heitor, M. V., and Shtork, S. I., 2003. "Swirl flow structure and flame characteristics in a model lean premixed combustor". Combustion Science and Technology, 175, p. 136988.
- [6] Syred, N., 2006. "A review of oscillation mechanisms and the role of the precessing vortex core (pvc) in swirl combustion systems". PECS 32(2), pp. 93–161.

- [7] Qureshi, I., Smith, A. D., and Povey, T., 2012. "Hp vane aerodynamics and heat transfer in the presence of aggressive inlet swirl". *J. Turbomach.* 135(2), 021040.
- [8] Qureshi, I., Beretta, A., Chana, K. S., and Povey, T., 2012. "Effect of aggressive inlet swirl on heat transfer and aerodynamics in an unshrouded transonic hp turbine". *J. Turbomach.* 134(6), 061023.
- [9] Cha, C. M., Hong, S., Ireland, P. T., Denman, P., and Savarianandam, V., 2012. "Turbulence levels are high at the combustor-turbine interface". *Proceedings of the ASME Turbo Expo GT2012-69130*.
- [10] Cha, C. M., Hong, S., Ireland, P. T., Denman, P., and Savarianandam, V., 2012. "Experimental and numerical investigation of combustor-turbine interaction using an isothermal, nonreacting tracer". *Journal of Engineering for Gas Turbines and Power*, 134(8), p. 081501.
- [11] Ames, F. E., Wang, C., and Barbot, P. A., 2003. "Measurement and prediction of the influence of catalytic and dry low nox combustor turbulence on vane surface heat transfer". *Journal of Turbomachinery*, 125(2), 04, pp. 221–231.
- [12] Salvadori, S., Riccio, G., Insinna, M., and Martelli, F., 2012. "Analysis of combustor/vane interaction with decoupled and loosely coupled approaches". *Proceedings of ASME Turbo Expo GT2012-69038*, 6.
- [13] Khanal, B., He, L., Northall, J., and Adami, P., 2013. "Analysis of radial migration of hot-streak in swirling flow through high-pressure turbine stage". *Journal of Turbomachinery*, 135(4), 06, pp. 041005–041005.
- [14] Schildmacher, K. U., and Koch, R., 2005. "Experimental investigation of the interaction of unsteady flow with combustion". *J. Eng. Gas Turbines Power* 127(2), 295–300.
- [15] Dawson, J. R., Rodriguez-Martinez, V. M., Syred, N., and O'Doherty, T., 2006. "The effect of combustion instability on the structure of recirculation zones in confined swirling flames". *Combust. Sci. and Tech.*, 177, pp. 2349–2371.
- [16] Turrell, M. D., Stopford, P. J., Syed, K., and Buchanan, E., 2004. "Cfd simulations of the flow within and downstream of high swirl lean premixed gas turbine combustors". *Proceedings of ASME Turbo Expo GT2004-53112*.
- [17] Schluter, J., Schonfeld, T., Poinso, T., Krebs, W., and Hoffman, S., 2001. "Characteristics of confined swirl flows using large eddy simulations". *ASME Turbo Expo 2001GT-0060*.
- [18] Takahashi, R., and Ni, R., 1990. "Unsteady euler analysis of the redistribution of an inlet temperature distortion in a turbine". *AIAA Paper No. 90-2262*.
- [19] You, D., Ham, F., and Moin, P. "Large-eddy simulation analysis of turbulent combustion in a gas turbine engine combustor". *Center for Turbulence Research; Annual Research Briefs 2008*.
- [20] Wang, P., Bai, X. S., and Wessman, M., 2004. "Large eddy simulation and experimental studies of a confined turbulent swirling flow". *Physics of Fluids*, 16(9), pp. 3306–3324.
- [21] Wang, S., Yang, V., Hsiao, G., Hsieh, S., and Mongia, C., 2007. "Large eddy simulations of gas-turbine swirl injector flow dynamics". *J Fluid Mech*, 583, pp. 99–122.
- [22] Hall, B., Chana, K., and Povey, T., 2014. "Design of a non-reacting combustor simulator with swirl and temperature distortion with experimental validation". *J. Eng. Gas Turbines Power* 136(8), p.081501.
- [23] Cameron, C., Brouwer, J., Wood, C., and Samuelsen, G., 1989. "A detailed characterization of the velocity and thermal fields in a model can combustor with wall jet injection". *J. of Eng. for Gas Turbines and Power*, 111, pp. 31–35.

- [24] Goebel, S., Abuaf, N., Lovett, J., and Lee, C., 1993. "Measurements of combustor velocity and turbulence profiles". ASME Paper No. 93-GT-228.
- [25] Roux, S., Lartigue, G., and Poinso, T., 2005. "Studies of mean and unsteady flow in a swirled combustor using experiments, acoustic analysis, and large eddy simulations". *Combustion and Flame*, 141(12), pp. 40–54.
- [26] Selle, L., Benoit, L., Poinso, T., Nicoud, F., and Krebs, W., 2006. "Joint use of compressible large eddy simulation and helmholtz solvers for the analysis of rotating modes in a industrial swirled burner". *Combustion and Flame*, 145, p. 194205.
- [27] Wankhede, M. J., Bressloff, N. W., Keane, A. J., Caracciolo, L., and Zedda, M., 2010. "An analysis of unstable flow dynamics and flashback mechanism inside a swirl-stabilised lean burn combustor". *Proceedings of ASME Turbo Expo GT2010-22253*.
- [28] O'Connor, J., and Lieuwen, T., 2011. "Further characterization of the disturbance field in a transversely excited swirl-stabilized flame". *J. Eng. Gas Turbines Power* 134(1), 011501.
- [29] Selle, L., Lartigue, G., Poinso, T., Koch, R., Schildmacher, K. U., and Krebs, W., 2004. "Compressible large eddy simulation of turbulent combustion in complex geometry on unstructured meshes". *Combustion and Flame*, 137, pp 489505.
- [30] Lubbock, R., 2013. "Fast insertion probes for unsteady temperature and turbulence measurements". DPhil Thesis, Department of Engineering Science, University of Oxford.
- [31] Moss, R., 1992. "The effects of turbulence length scale on heat transfer". Ph.D. Dissertation, Department of Eng. Sc., University of Oxford, Report No. OUEL 1924/92.
- [32] Zimmerman, D. R., 1979. "laser anemometer measurements at the exit of a t63-c20 combustor". NASA, Contract NAS 3-21267.
- [33] Barringer, M. D., Richard, O. T., Walter, J. P., Stitzel, S. M., and Thole, K. A., 2002. "Flow field simulations of a gas turbine combustor". *J. Turbomach* 124(3), pp. 508–516.
- [34] Luque, S., Kanjirakkad, V., Aslanidou, I., Lubbock, R., and Rosic, B., 2015. "A new experimental facility to investigate combustor-turbine interactions in gas turbines with multiple can combustors". *J. Eng. Gas Turbines Power* 137(5), 051503.
- [35] Roach, P., 1987. "The generation of nearly isotropic turbulence by means of grids". *International Journal of Heat and Fluid Flow*, 8(2), pp. 82 – 92.
- [36] Oldfield, M., 2008. "Impulse response processing of transient heat transfer gauge signals". *Journal of Turbomachinery*, 130(2), pp. 021023(1-9).
- [37] Doorly, J., and Oldfield, M., 1987. "The theory of advanced multi-layer thin film heat transfer gauges". *International Journal of Heat Mass Transfer*, 30 (6), pp. 1159–1168.
- [38] Piccini, E., 1999. "The development of a new heat transfer gauge for heat transfer facilities". Univeristy of Oxford D.Phil Thesis.
- [39] Denton, J. D., 1983. "An improved time-marching method for turbomachinery flow calculation". *Journal for Engi-*

- neering for Power, 105(3), 07, pp. 514–521.
- [40] Klostermeier, C., 2008. Investigation into the Capability of Large Eddy Simulation for Turbomachinery Design. PhD Thesis, Cambridge University Engineering Department.
- [41] Mazzoni, C., Luque, S., and Rosic, B., 2015. “Capabilities of thermal wall functions to predict heat transfer on the ngvs of a gas turbine with multiple can combustors”. ASME Turbo Expo GT2015-43515.
- [42] Jacobi, S., 2013. Influence of Lean Premixed Combustor Geometry on the First Turbine Vanes’ Aerothermal Performance. ETH Zurich; Department of Mechanical and Process Engineering.
- [43] SHARCNET. Lambda 2 definition. [https://www.sharcnet.ca/Software/Ansys/16.0/en-us/help/cfd\\_post/vort-core\\_details\\_v.html](https://www.sharcnet.ca/Software/Ansys/16.0/en-us/help/cfd_post/vort-core_details_v.html).
- [44] Jeong, J., and Hussain, F., 1995. “On the identification of a vortex”. Journal of Fluid Mechanics, 285, 2, pp. 69–94.
- [45] Richards, A. University of oxford advanced research computing facility. <http://dx.doi.org/10.5281/zenodo.22558>.

Condition	Value
NGV inlet total p = T	$p_{01} = 1.6 \text{ bar} / T_{01} = 320\text{K}$
NGV pressure ratio	$\frac{p_2}{p_{01}} = 0.75$
NGV exit Mach number	$M_2 = 0.65$
Mass flow rate	$m = 4.8 \text{ kg/s}$
NGV Reynolds no. (based on $c_x$ )	$Re_x = 1.6 \cdot 10^6$
Inlet turbulence intensity	$Tu = 10 - 20\%$

Table 1: Experimental conditions

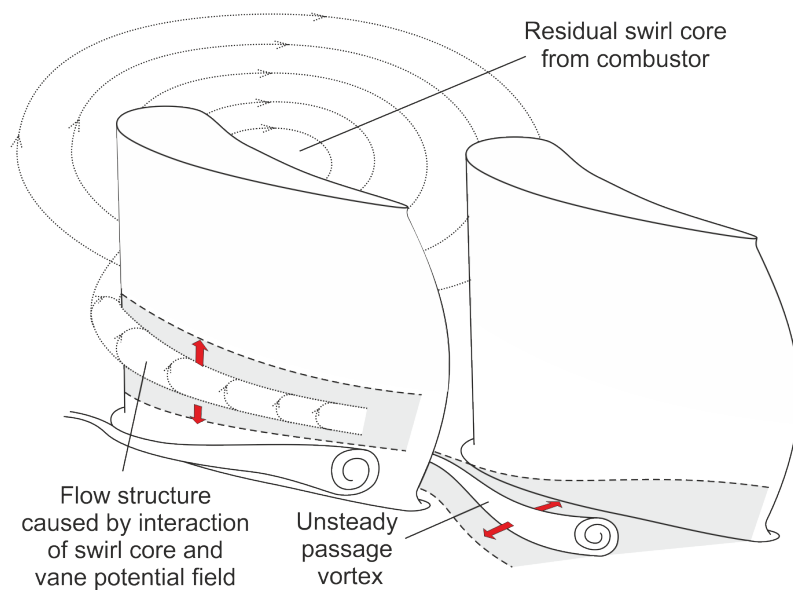


Fig. 1: Schematic of unsteady interaction between residual swirl core and vane's potential field, and of unsteady nature of passage vortex

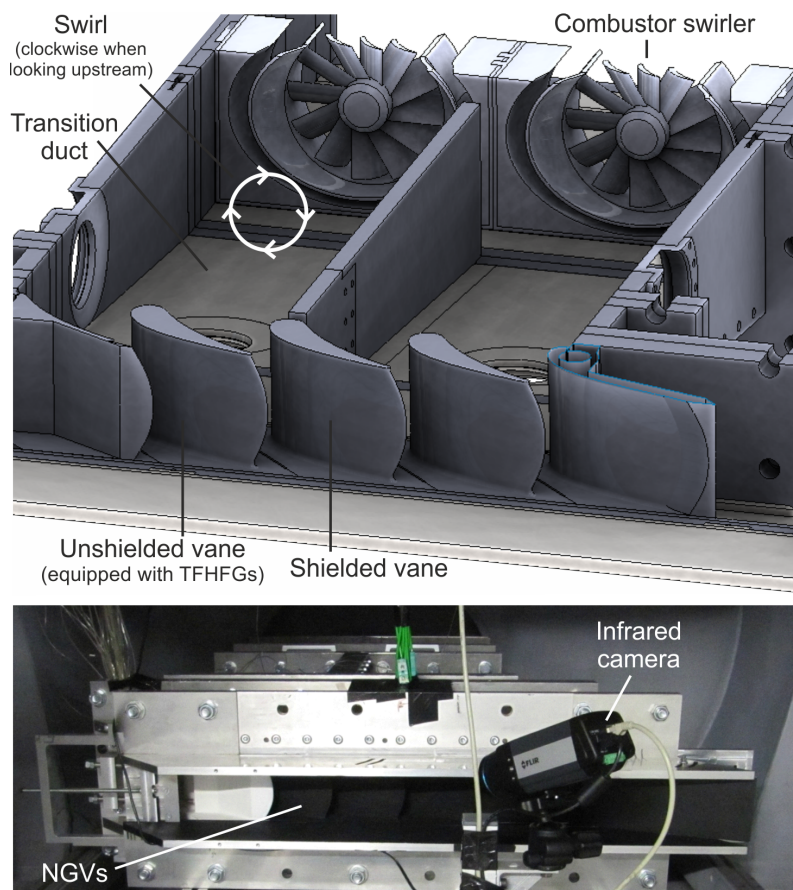


Fig. 2: CAD (top) and photo (bottom) of the experimental facility's working section (view from downstream), including swirlers, transition ducts and nozzle guide vanes

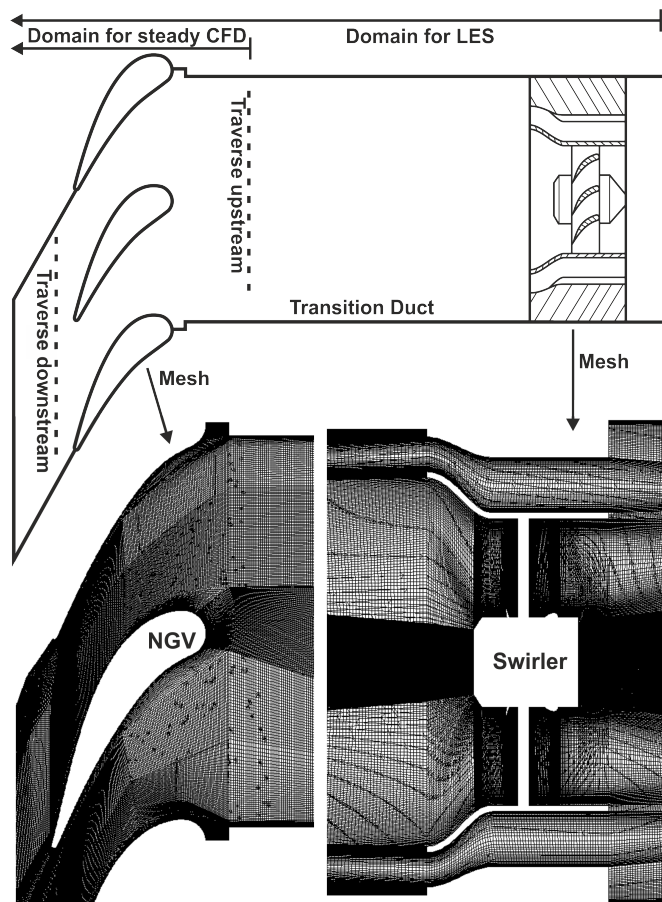


Fig. 3: Schematic of computational domain for steady CFD and LES; horizontal cut at midspan illustrating structured mesh for LES of swirler and vane passages

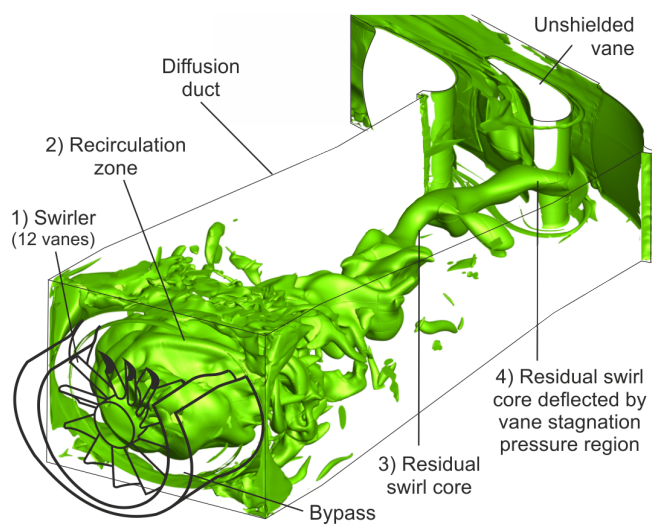


Fig. 4: Iso-surface of total pressure obtained from instantaneous time step of LES

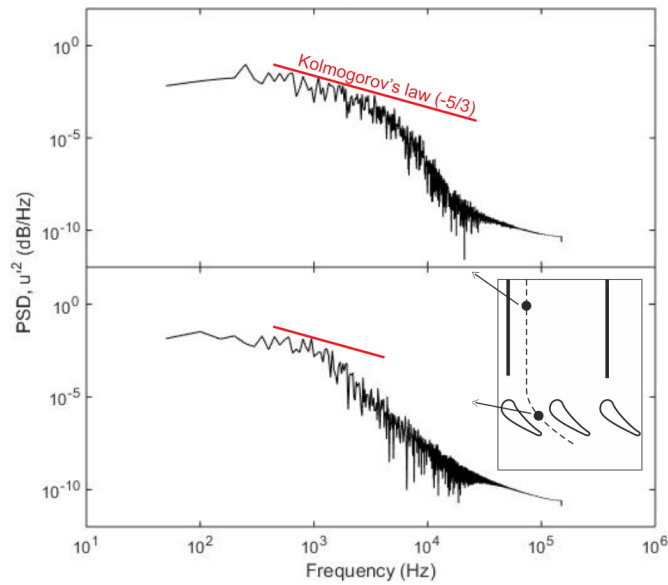


Fig. 5: Energy cascade of LES for two midspan points in the computational domain

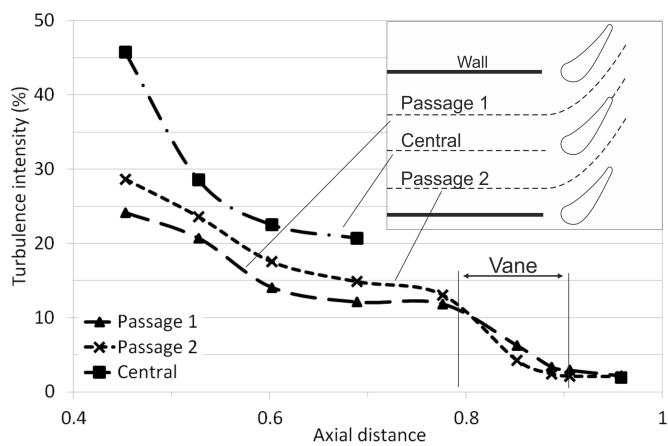


Fig. 6: Turbulence intensity within transition duct and vane passages at midspan (time-averaged LES)

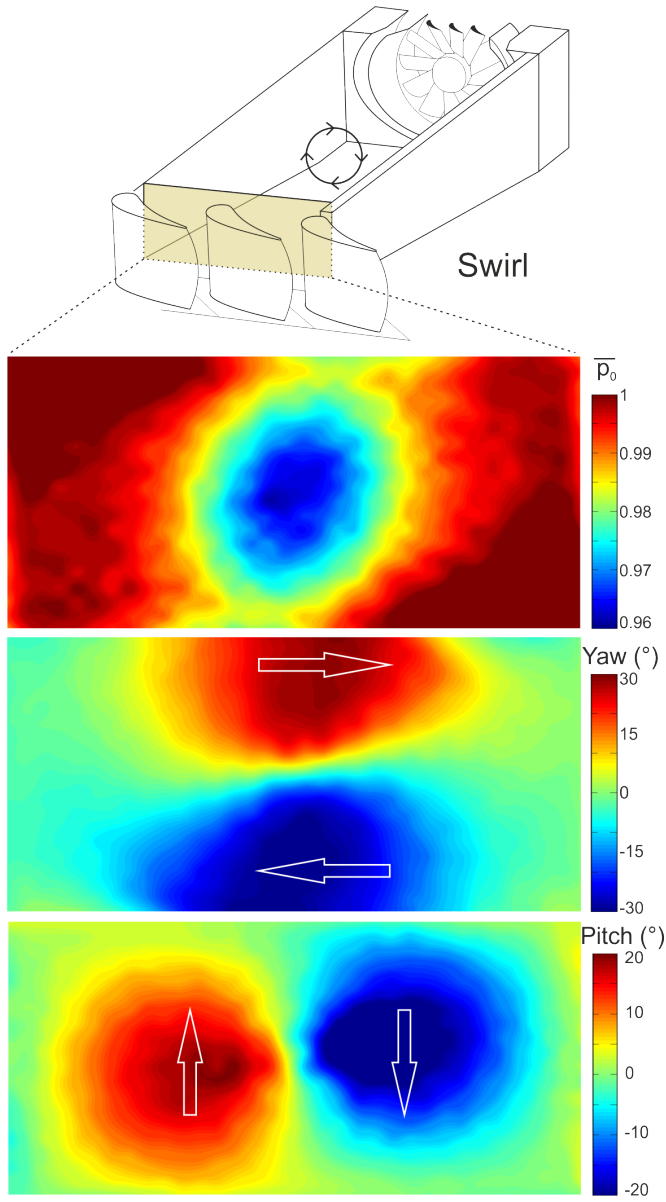


Fig. 7: Dimensionless total pressure (top), yaw (middle) and pitch (bottom) distributions downstream of the transition duct; obtained through traverse measurements with installed swirler



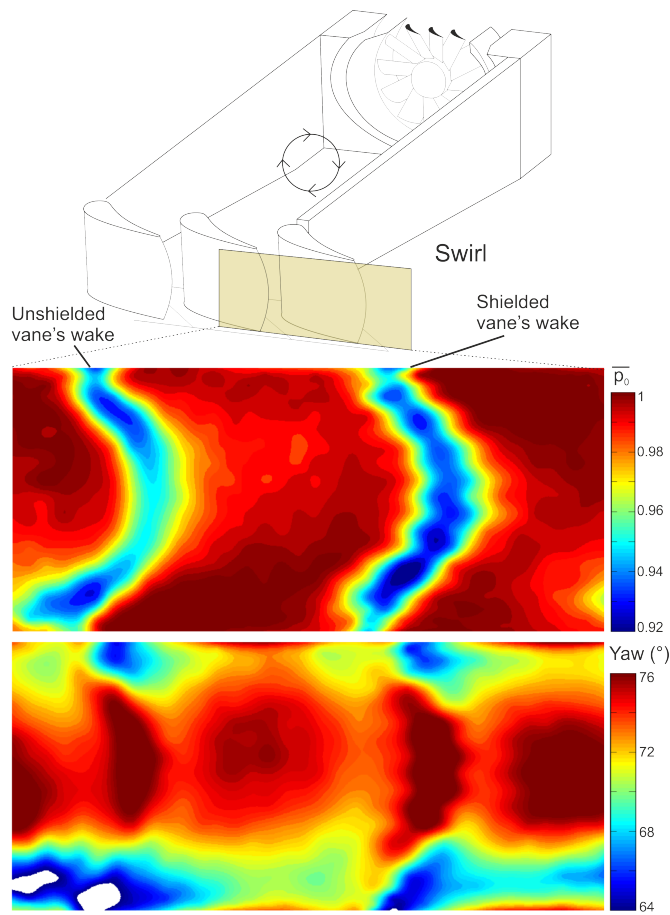


Fig. 8: Dimensionless total pressure (top) and yaw (bottom) distributions downstream of the nozzle guide vanes; obtained through traverse measurements with installed swirler

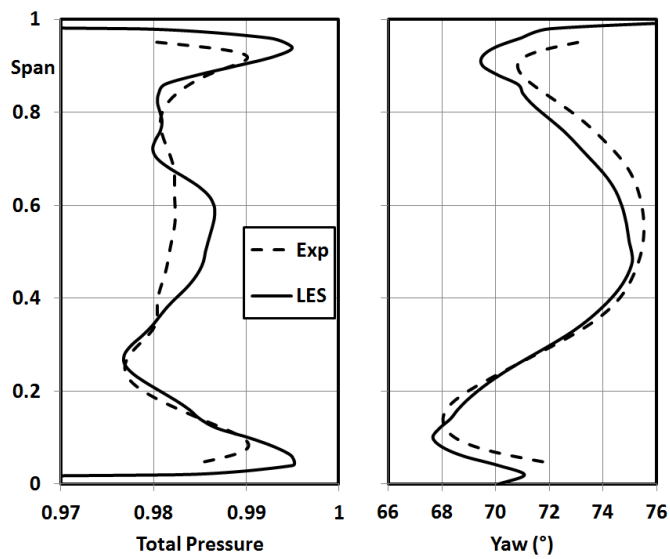


Fig. 9: Pitchwise averaged dimensionless total pressure (left) and yaw (right) downstream of the nozzle guide vanes for experimental measurements (dashed) and time-averaged LES (solid); with swirler

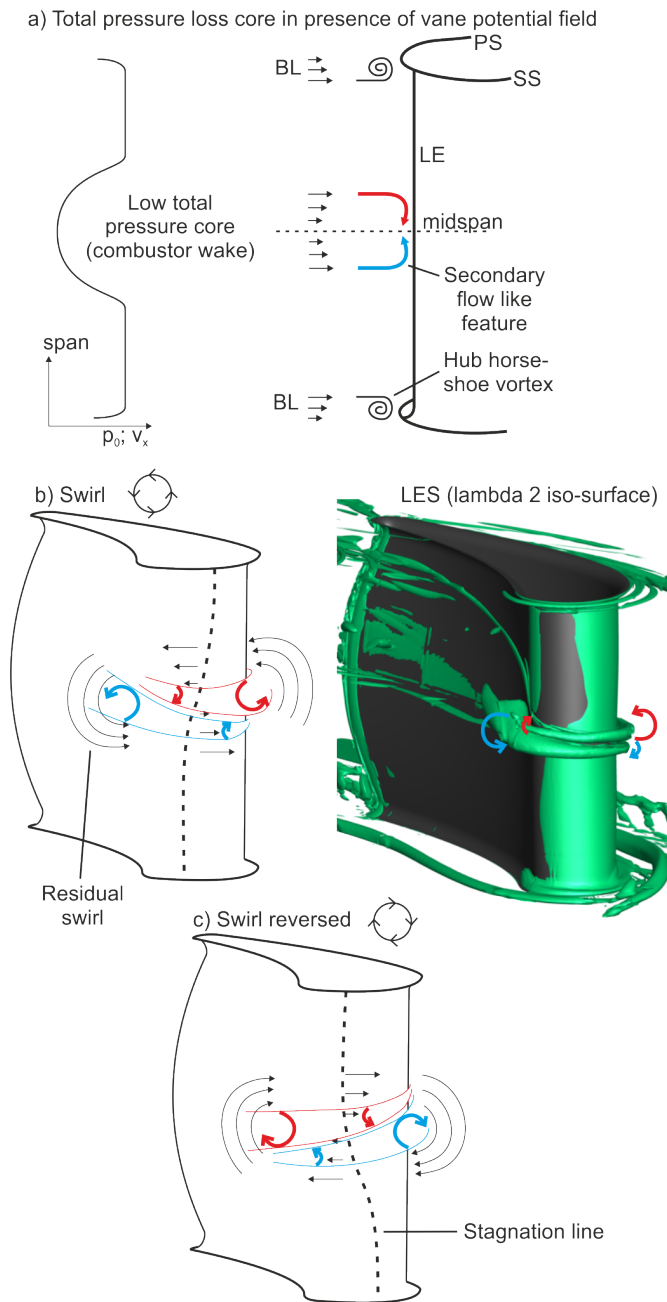


Fig. 10: Schematic of interaction between residual swirl core and vane potential field

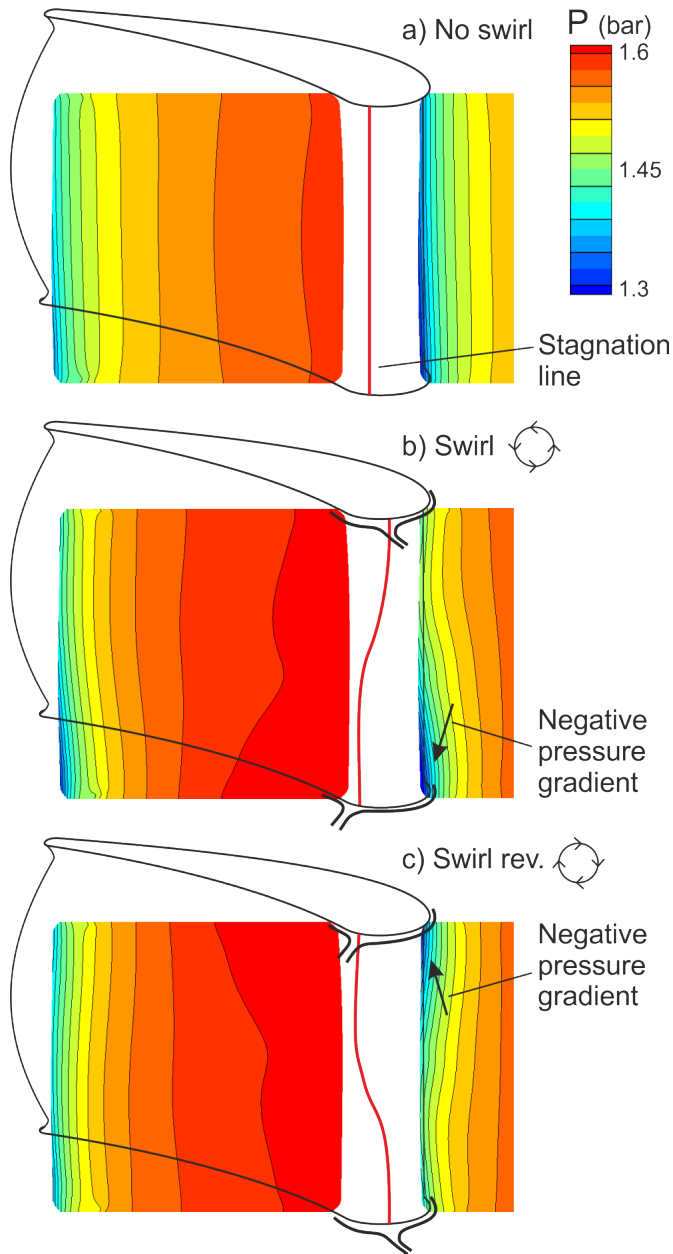


Fig. 11: Static pressure contour and stagnation line at unshielded vane's leading edge for a no swirl (top), swirl (middle) and reversed swirl (bottom) case; based on steady CFD

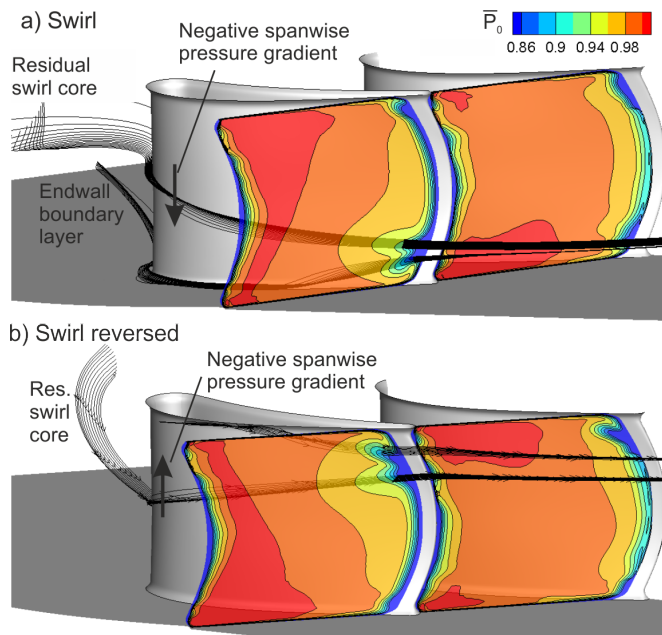


Fig. 12: Dimensionless total pressure distribution at vanes trailing edges for swirl (top) and reversed swirl (bottom) scenario; streamtraces of residual swirl core and endwall boundary layer; steady CFD

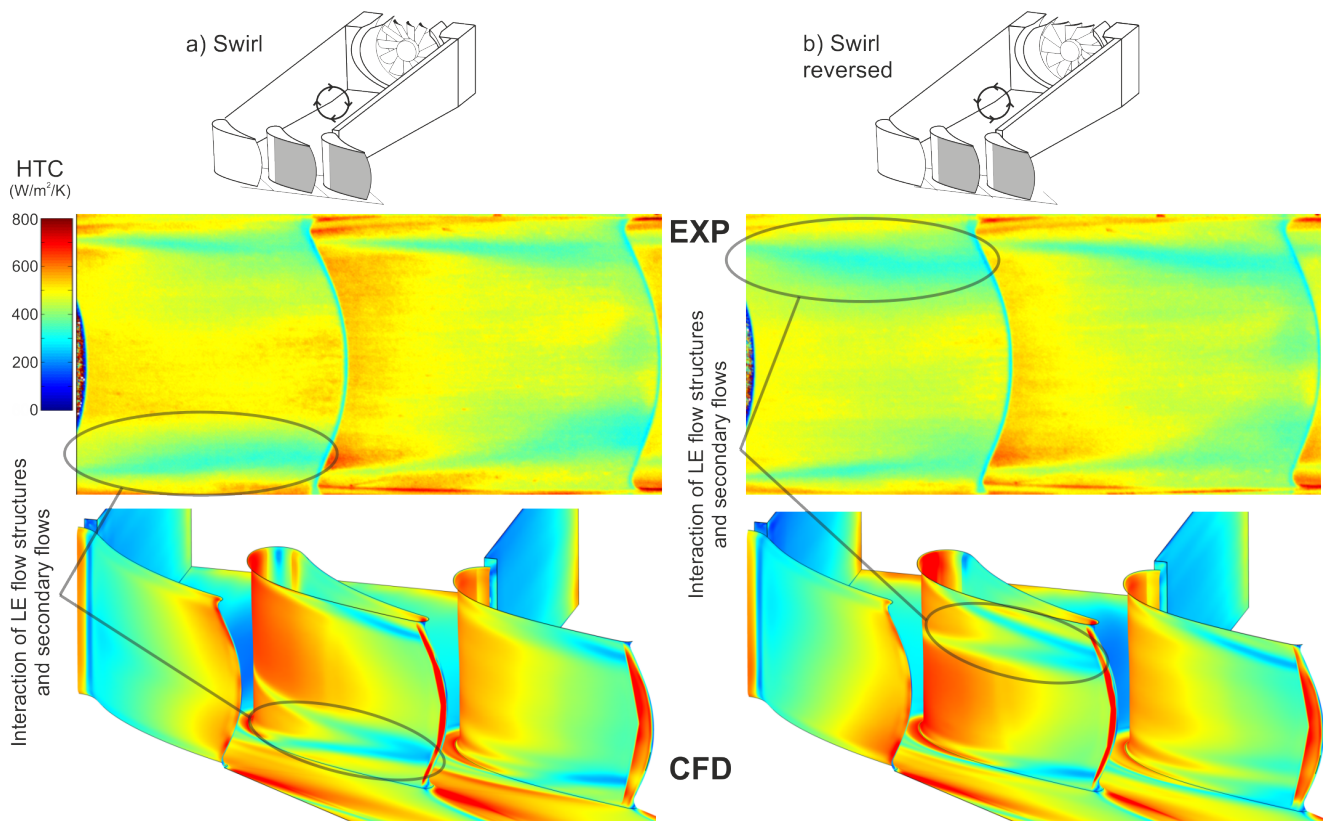


Fig. 13: Heat transfer coefficient distributions on the vanes suction surfaces obtained from experimental measurements (top) and steady CFD simulations (bottom) for a swirl (left) and reversed swirl (right) case

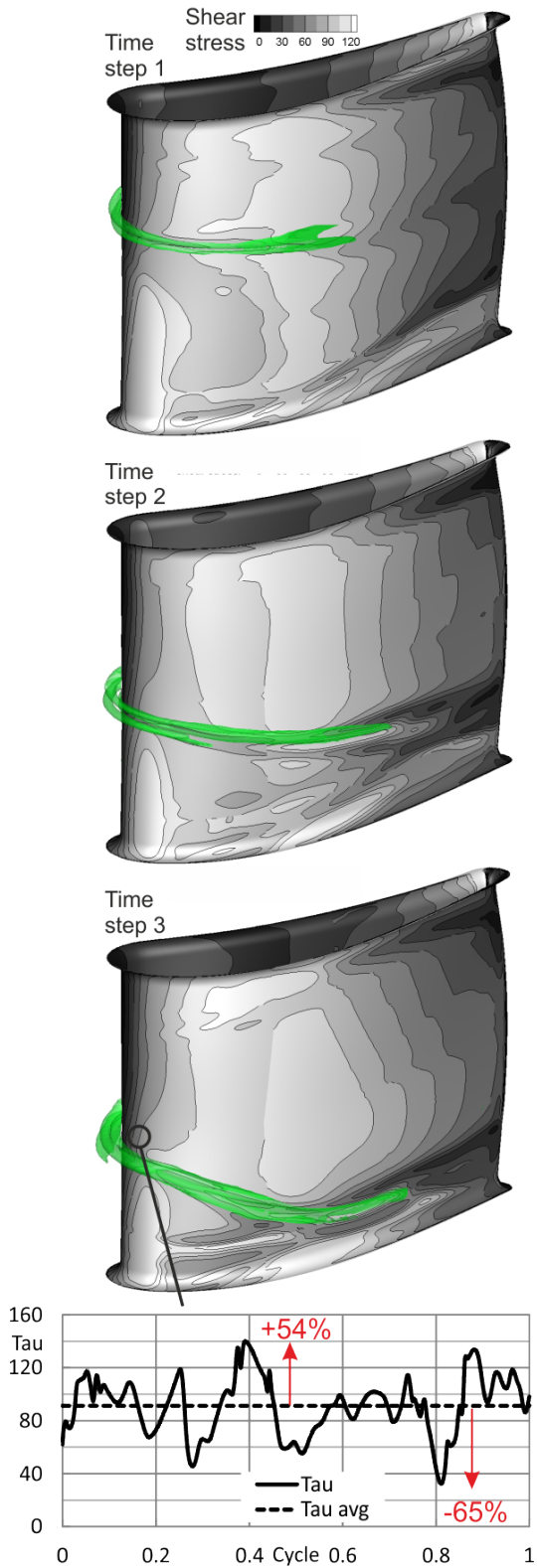


Fig. 14: Wall shear stress on unshielded vane's suction surface for three time steps with iso-surface of  $\lambda_2$  criterion (top); graph of wall shear stress for a point on the leading edge over time (bottom)

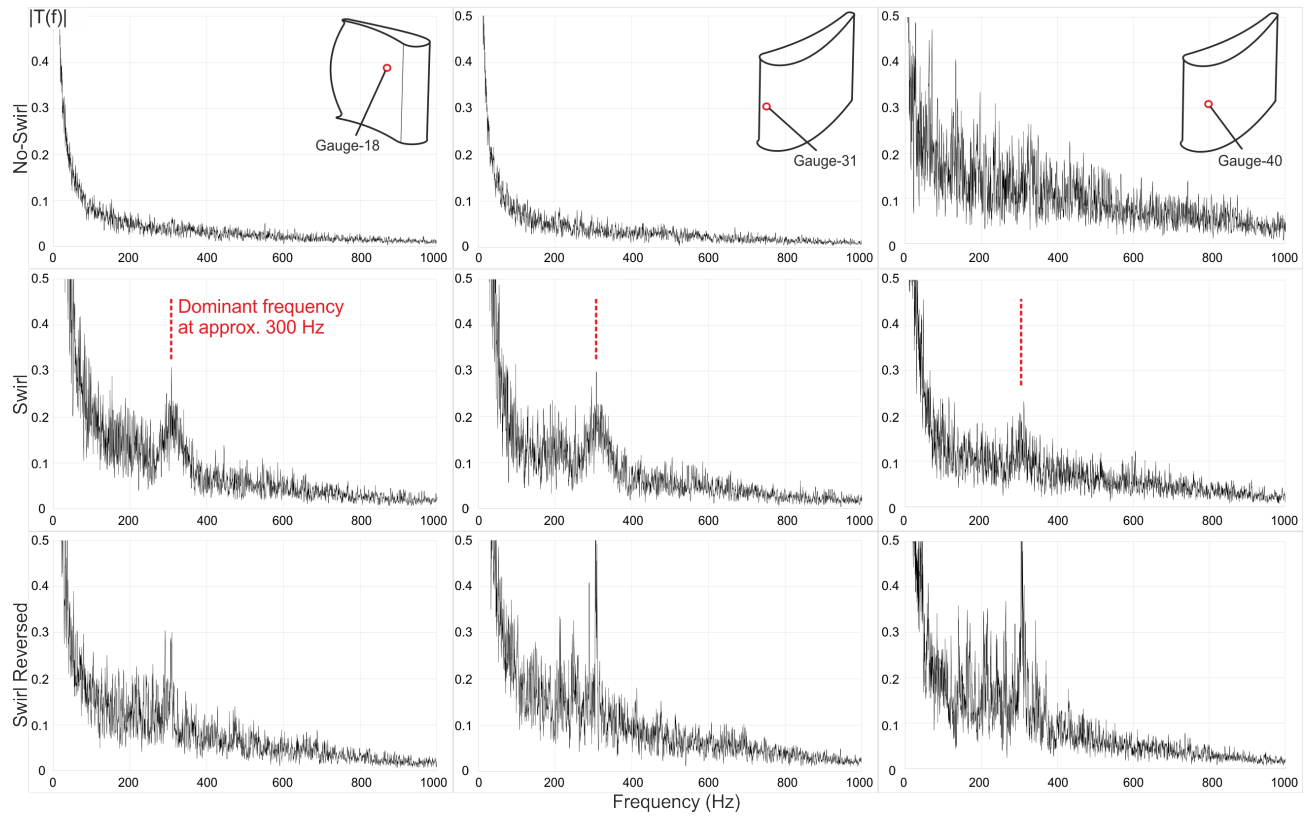


Fig. 15: Discrete Fourier Transformation of unshielded vane's temperature obtained from experimental thin-film gauge measurements on the pressure side (left), leading edge (middle) and suction side (right) for a no swirl (top), swirl (middle) and reversed swirl (bottom) scenario

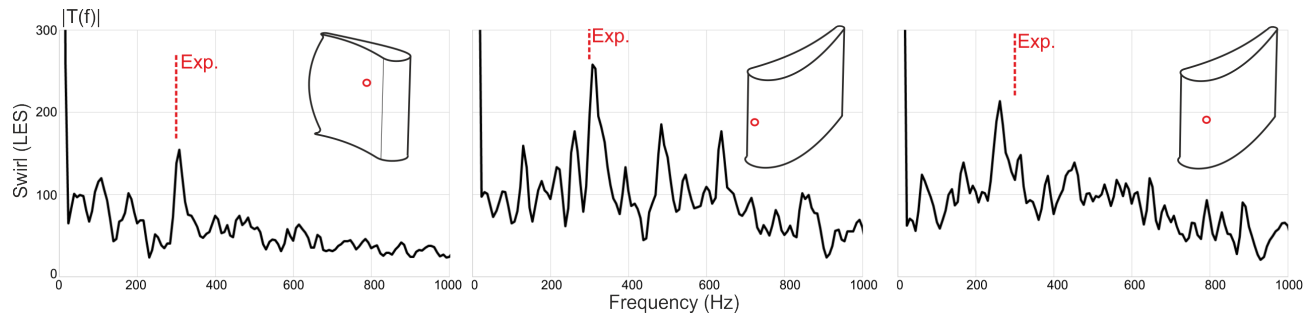


Fig. 16: Discrete Fourier Transformation of unshielded vane's heat flux obtained from LES for point on the pressure side (left), leading edge (middle) and suction side (right) for the swirl scenario

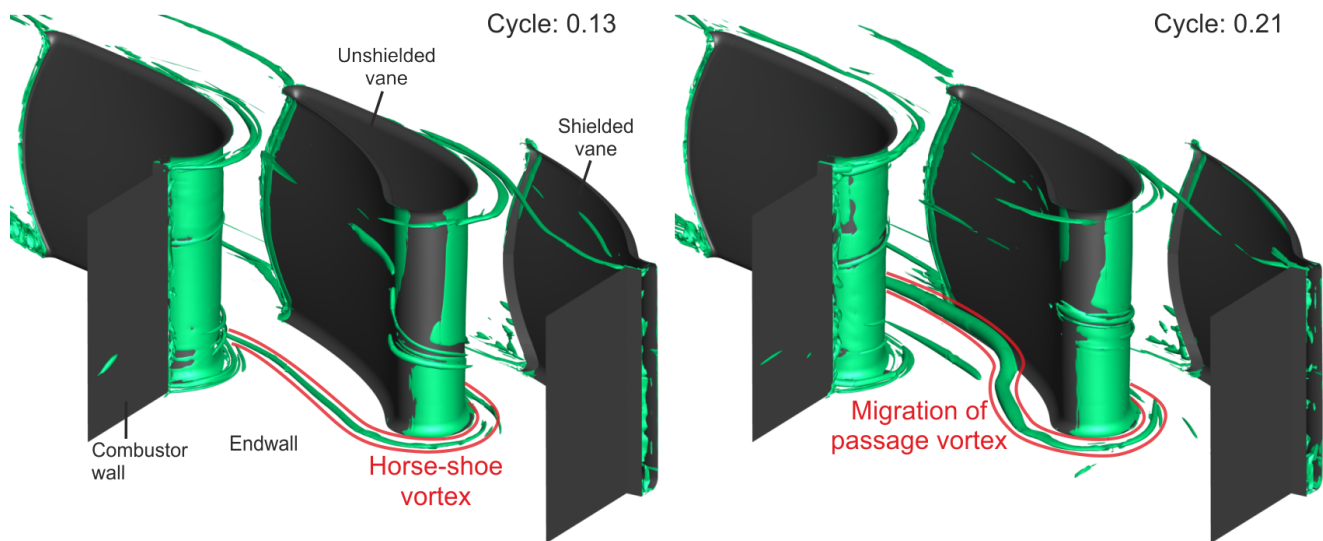


Fig. 17: Iso-surface of lambda 2 criterion in vane passages

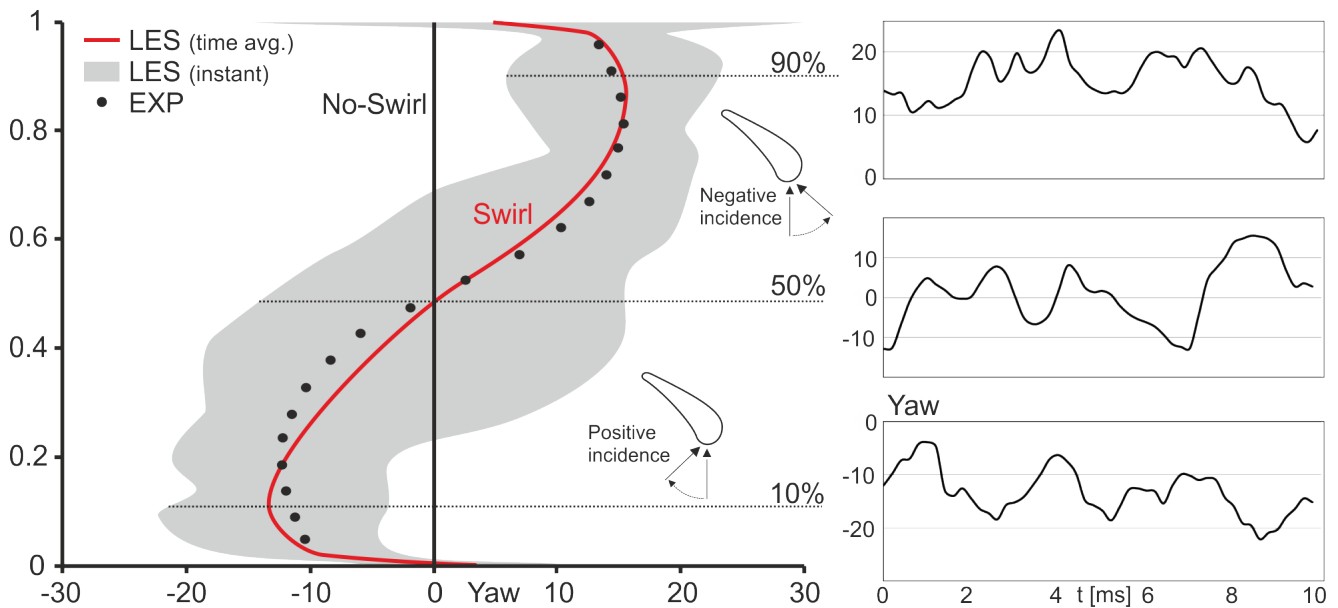


Fig. 18: Unsteadiness of upstream pitchwise-averaged yaw



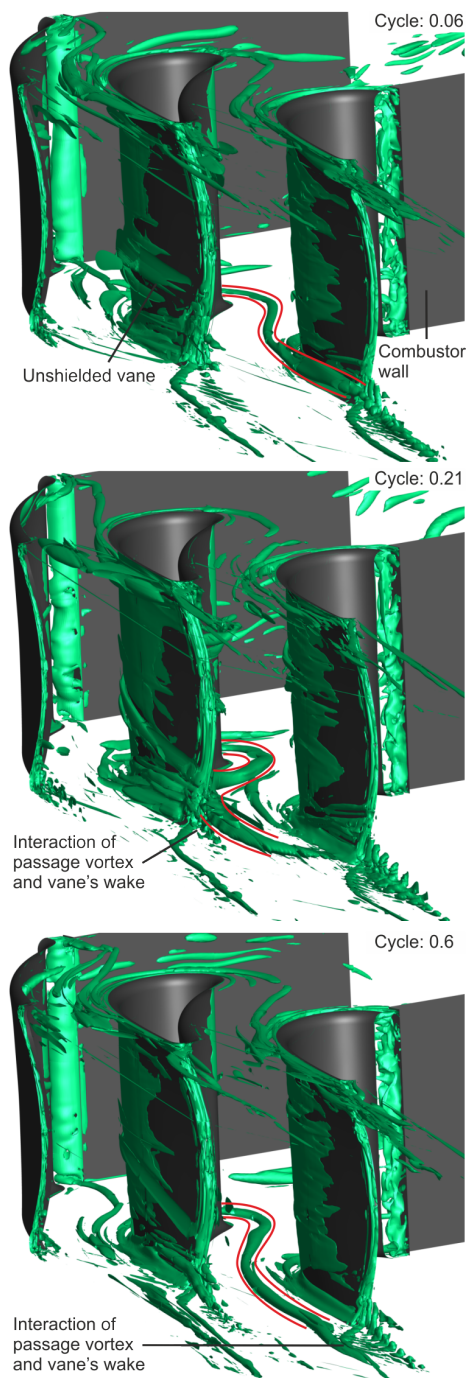


Fig. 19: Iso-surface of lambda 2 criterion in vane passages; looking from downstream